Applied Catalysis B: Environmental 300 (2022) 120738

Contents lists available at ScienceDirect

Applied Catalysis B: Environmental

journal homepage: www.elsevier.com/locate/apcatb

One-step hydrothermal synthesis of $Cd_xIn_yS_{(x+1.5y)}$ for photocatalytic oxidation of biomass-derived 5-hydroxymethylfurfural to 2, 5-diformyl-furan under ambient conditions

Ming Zhang [a], Zhihao Yu [a], Jian Xiong [b], Rui Zhang [c], Xinzhong Liu [d], Xuebin Lu [a,b,*]

[a] School of Environmental Science & Engineering, Tianjin University, Tianjin 30000, PR China
[b] School of Science, Tibet University, Lhasa 850000, PR China
[c] School of Environmental and Municipal Engineering, Tianjin Chengjian University, Tianjin 300384, PR China
[d] School of Ecological Environment and Urban Construction, Fujian University of Technology, Fuzhou 350000, PR China

ARTICLE INFO

Keywords:
Cadmium–indium sulfides
Photocatalysis
CdS nanorods
$\bullet O_2^-$
Ambient conditions

ABSTRACT

The $Cd_xIn_yS_{(x+1.5y)}$ catalysts with gradient Cd:In ratios were controllably synthesized via an one-step hydrothermal approach. Particularly, the hydrothermal synthesis conferred those $Cd_xIn_yS_{(x+1.5y)}$ catalysts with Cd:In ratios over 1:2 with a one-dimensional–three-dimensional heterojunction structure composed of CdS nanorods and cubic-phase $CdIn_2S_4$. Our characterization evidences reflected that the CdS nanorods effectively promoted the separation of photoexcited electron–hole pairs in $Cd_xIn_yS_{(x+1.5y)}$ and enabled transboundary transfer of photogenerated carriers. Spectroscopic and experimental results were further employed to develop a detailed catalytic mechanism, in which the superoxide anion ($\bullet O_2^-$) plays an important role in the catalytic oxidation of HMF to DFF by $Cd_xIn_yS_{(x+1.5y)}$. Unlike other photocatalysts with $\bullet O_2^-$ as the main active species, $Cd_{1.5}In_2S_{4.5}$ gives an excellent performance in HMF conversion. This shows the great potential of cadmium–indium sulfides as photocatalysts for biomass conversion under ambient conditions.

1. Introduction

The selective oxidation of 5-hydroxymethylfurfural (HMF) to 2,5-diformylfuran (DFF) is a pivotal step towards high-value products chemically synthesized from renewable biomass feedstocks [1–3]. DFF, an important downstream product of HMF [3–5], contains two active aldehyde groups and a furan ring, which can be further transformed into industrial chemicals and macromolecular materials, e.g., medicines, organic conductors, fluorescent agents, and macrocyclic ligands, via hydrogenation, oxidation, polymerization, hydrolysis, and other processes [5–7]. Over the past decade, various approaches such as thermal-catalytic oxidation and electro-catalytic oxidation had been investigated for the selective conversion of HMF to DFF [8–11]. However, traditional chemical oxidation techniques usually required harsh temperatures and high pressures [2,12], which tend to result in various safety risks and environmental concerns[6,13]. Developing environmentally friendly catalytic systems for the oxidation of HMF to DMF with high efficiency under mild conditions is considered urgent for production practices. Eagerly, the desired catalytic system should avoid utilizing hazardous chemicals (substrates or organic solvents), and meanwhile favor budget nonprecious-metal catalysts, mild oxidants, e.g., oxygen in the air, as well as room temperatures. With continuous research efforts, the photocatalytic technology promises the above idea a higher possibility to become a reality [1–3,6,14,15].

Photocatalytic methods use clean and renewable solar energy and are therefore more environmentally friendly than traditional chemical oxidation techniques [16,17]. The photocatalytic conversion of renewable resources to value-added chemicals is important in terms of green chemistry and sustainable development [18–20]. In recent years, investigations on the photocatalysis for the selective oxidation of HMF to DFF have been gradually performed [1,2,21]. In 2013, Yurdakal et al. [22] reported the first use of anatase TiO_2 in the catalytic conversion of HMF in an aqueous medium, with an ultraviolet (UV) light source. The main organic product was DFF, but the selectivity was low (10–25%). Wu et al. [23] reported the catalytic oxidation of HMF to DFF with Nb_2O_5 in trifluorobenzene as the solvent under visible light. The DFF yield was 20%. Giannakoudakis et al. [24] achieved UV-promoted oxidation of HMF to DFF by using MnO_2 nanorods as the catalyst and

* Correspondence to: School of Environmental Science & Engineering, Tianjin University, School of Science, Tibet University.
E-mail address: xbltju@tju.edu.cn (X. Lu).

https://doi.org/10.1016/j.apcatb.2021.120738
Received 23 July 2021; Received in revised form 16 September 2021; Accepted 19 September 2021
Available online 22 September 2021

acetonitrile as the reaction medium. HMF was almost completely converted to DFF without the addition of any oxidant or alkali. The selective catalytic oxidation of HMF with metal sulfide catalysts has also been reported. In 2017, Sun et al. [25] evaluated the catalytic activity Ni-loaded CdS nanosheets in the photocatalytic conversion of HMF to DFF. They reported that the Ni/CdS catalyst achieved 20% HMF conversion with 90% DFF selectivity after a cavitation (h^+) reaction for 22 h. Metal sulfides are dynamic semiconductor photocatalysts [26,27]. Unlike the case for metal oxides, the photogenerated carriers in metal sulfides are usually smaller than the effective mass of metal sulfides [28]. This indicates that metal sulfides have higher hole mobility and give better charge transfer. Many metal sulfides have relatively small bandgaps and their solar spectra are wider than those of metal oxides [15]. The morphology and size of wurtzite CdS can be controlled by changing the synthetic conditions and materials. Among CdS materials with different morphologies, one-dimensional CdS nanorods have attracted much attention because of their radial quantum limitation and axial blocking characteristics, which promote the rapid generation and separation of photogenerated carriers [29,30]. $CdIn_2S_4$, which is a narrow bandgap semiconductor, has attracted extensive attention because it has applications in various fields [31,32]. The bandgaps of CdS and $CdIn_2S_4$ are approximately 2.4 and 2.3 eV, respectively [33], and they have appropriate valence band and conduction band potentials for use in the selective oxidation of HMF to DFF. One-dimensional CdS nanorods have special quantum limitation and axial blocking characteristics, and this heterostructure favors transboundary transfer of photonic carriers. The efficiency of the catalytic conversion of HMF could therefore be improved by using a composite material. However, the photocatalytic transformation of HMF by one-dimensional CdS nanorods, $CdIn_2S_4$, and $Cd_xIn_yS_{(x+1.5y)}$, and the catalytic mechanism, have not been studied.

Herein this paper, a $Cd_xIn_yS_{(x+1.5y)}$ photocatalyst consisting of one-dimensional CdS nanorods and three-dimensional cubic-phase $CdIn_2S_4$ was prepared by a one-step hydrothermal method. This photocatalyst was proved to exhibit satisfactory performance for the selective oxidation of HMF in water under ambient conditions, without high temperatures, pressures, and additives. The differences among the morphologies and photoactivities of $Cd_xIn_yS_{(x+1.5y)}$ samples with different Cd:In ratios were investigated, and the importance of $\bullet O_2^-$ formation in the system was confirmed. A possible mechanism for the photocatalytic oxidation of HMF to DFF by $Cd_xIn_yS_{(x+1.5y)}$ was further proposed. Our experimental and characterization evidences demonstrated that $Cd_xIn_yS_{(x+1.5y)}$ composites have shown promising potentials as photocatalysts for selective oxidation of biomass-derived HMF.

2. Experimental

2.1. Materials

Indium nitrate tetrahydrate ($In(NO_3)_3\bullet 4H_2O$), cadmium nitrate tetrahydrate $Cd(NO_3)_2\bullet 4H_2O$, Thioacetamide (TAA), Ethanol, HMF and other experimental reagents were purchased from Shanghai Aladdin Chemical Reagent Co., Ltd. All of the reagents were analytical grade without further purification. Deionized water was used throughout this study.

2.2. Preparation of $Cd_xIn_yS_{(x+1.5y)}$ composites

$Cd_xIn_yS_{(x+1.5y)}$ metal sulfide is synthesized by one-step hydrothermal method. Take $C_{1.5}In_2S_{4.5}$ as an example, 0.34 g TAA were successively dissolved in 70 mL deionized water under continuous stirring. Then, 0.46 g $Cd(NO_3)_2\bullet 4H_2O$, 0.64 g $In(NO_3)_3\bullet 4H_2O$ were added into the above solution. After stirring for 30 min, the solution was transferred into a 100 mL Teflon-lined autoclave (Anhui Kemi Machinery Technology Co., Ltd.) and heated at 180 °C for 20 h. Finally, the precipitate was washed with absolute ethanol and deionized water for several times and dried at 60 °C in a vacuum oven. The $Cd_xIn_yS_{(x+1.5y)}$ metal sulfide was obtained. By changing the amount of $Cd(NO_3)_2\bullet 4H_2O$ and $In(NO_3)_3\bullet 4H_2O$, $Cd_xIn_yS_{(x+1.5y)}$ with different Cd and In content ratios are synthesized.

2.3. Characterization

The powder X-ray diffraction (XRD) patterns of the samples were collected on a Bruker D8 Advance X-ray diffractometer with Cu-Kα radiation and a scanning speed of 3°/min at room temperature. High resolution scanning electron microscope (HR-SEM) FEI Nova Nano SEM 450 was used to determine the morphology of the $Cd_xIn_yS_{(x+1.5y)}$. UV–vis diffuse reflectance spectra of the obtained samples were carried out using a UV-3600 (SHIMA-DZU, Japan). Transmission electron microscope (TEM) and high-resolution transmission electron microscope (HR-TEM) images were performed with a TecnaiG2F20S-TWIN electron microscope with an accelerating voltage of 200 kV. All of electrochemical experiments were performed with a CHI-660E electrochemical workstation (Shanghai Chenhua Instruments Co., Ltd.). Electron spin resonance (ESR) signals of spin-trapped paramagnetic species with 5,5-dimethyl-1-pyrroline-N-oxide (DMPO) were detected using a Bruker A300E spectrometer. The components of products in the reaction system were analyzed by LC-MS-900 (Shimadzu, Japan). TOC-L (Shimadzu, Japan) was used to analyze the change of total organic carbon content in the reaction system with hole capture.

2.4. Photocatalytic activity tests

Photoreactors were filled with aqueous HMF (5 mL, 20 mg) and the catalyst (20 mg). The irradiation protocol was as follows. Equilibration was performed for 30 min in the dark under vigorous stirring (500 rpm) to determine the possibility of adsorption and/or reactivity even in the dark. A xenon lamp (CEL-HXF3003-T3) equipped with a UV cut filter ($\lambda > 420$ nm) was switched on, a water condenser was connected, and the reaction system was kept at 20 ℃. Illumination and continuous stirring were performed for 6 h. Tests in hermetically sealed vials were performed on samples removed after 30 min and 6 h. The reactants and products were analyzed with a Waters high-performance liquid-chromatography system equipped with a dual-absorbance detector. A C18 AQ column was used; the mobile phase was 0.5 mmol/L sulfuric acid solution at a flow rate of 1 mL/min. The HMF conversion, DFF yield, and selectivity were calculated by using the following equation:

$$Con_{HMF} = \frac{C_{HMF,0} - C_{HMF}}{C_{HMF,0}} \bullet 100\%$$

$$Yield_{DFF} = \frac{C_{DFF}}{C_{HMF,0} - C_{HMF}} \bullet 100\%$$

$$Sele_{DFF} = \frac{C_{DFF}}{C_{HMF,0}} \bullet 100\%$$

where $C_{5\text{-HMF},0}$ is the concentration of HMF after dark reaction for 30 min, $C_{5\text{-HMF}}$ and C_{DFF} are molar amount of 5-HMF or DFF after the reaction, respectively.

3. Result and discussion

3.1. Catalyst characterization

The crystallographic structures of CdS, $CdIn_2S_4$, In_2S_3, and $Cd_xIn_yS_{(x+1.5y)}$ samples synthesized under similar conditions were investigated by XRD; the patterns are shown in Fig. 1. The diffraction peaks at ca. 24.81°, 26.51°, 28.18°, 43.68°, and 51.82° can be assigned to the (100), (002), (101), (110), and (112) crystallographic planes, respectively, of the hexagonal CdS phase (JCPDS NO.41-1049). The

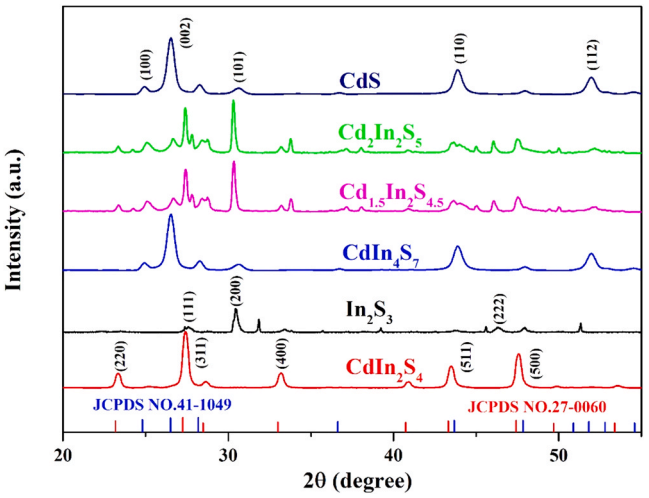

Fig. 1. XRD patterns of CdS, $CdIn_2S_4$, In_2S_3 and $Cd_xIn_yS_{(x+1.5y)}$.

diffraction peaks at 23.18°, 27.25°, 33.00°, 43.32°, and 47.41° can be assigned to the (220), (311), (400), (511), and (440) crystallographic planes, respectively, of the cubic $CdIn_2S_4$ phase (JCPDS NO.27-0060). The broad XRD peaks at $2\theta = 28.81°$, 33.43°, and 48.02° are assigned to the (111), (200), and (222) crystallographic planes of the hexagonal In_2S_3 phase (JCPDS NO.25-0390). The main diffraction peaks of CdS and $CdIn_2S_4$ are present in the patterns of the $Cd_{1.5}In_2S_{4.5}$ and $Cd_2In_2S_5$ composite samples, and the main diffraction peaks of In_2S_3 and $CdIn_2S_4$ can be observed in the $CdIn_4S_7$ composite sample pattern. This indicates that when Cd:In < 1:2, the material consists of $CdIn_2S_4$ and In_2S_3. When Cd:In > 1:2, the material consists of CdS and $CdIn_2S_4$.

The morphologies and microstructures of the prepared CdS, $CdIn_2S_4$, In_2S_3, and $Cd_xIn_yS_{(x+1.5y)}$ composites were studied by SEM and TEM. Fig. 2(a) shows that the one-dimensional CdS nanorods synthesized by a one-step hydrothermal method are of diameter approximately 20 nm. $CdIn_2S_4$ has a cubic structure of size approximately 50 μm. The $Cd_{1.5}In_2S_{4.5}$ sample self-organizes into a spherical morphology with a puffy appearance (Fig. 2a). A magnified image of the spherical surface shows that it is composed of a large amount of cubic $CdIn_2S_4$ and CdS nanorods (Fig. 2b). The EDS survey spectrum (Fig. 2e) shows that $Cd_{1.5}In_2S_{4.5}$ consists of Cd, In, and S. The Cd:In:S molar ratios in the $Cd_{1.5}In_2S_{4.5}$ sample are 26.52:19.13:54.35; this is in agreement with the theoretical molar ratios. The EDS mapping results (Fig. 2e) confirm that these three elements are uniformly distributed in the microstructure. The TEM images support the results of the SEM analysis. Fig. 2(f) shows that the interior of the spherical $Cd_{1.5}In_2S_{4.5}$ is composed of cubic-phase $CdIn_2S_4$ and CdS nanorods. The size of the CdS nanorods in $Cd_{1.5}In_2S_{4.5}$ is approximately 10 nm, which is significantly smaller than that of pure CdS. This is probably because the presence of $CdIn_2S_4$ crystals restricts the growth of CdS crystals during hydrothermal synthesis. Quantum confinement in the radial direction leads to diameter-dependent transition energies: the smaller the diameter, the smaller the transition energy [29]. The small CdS nanorods that are formed during the hydrothermal synthesis of $Cd_{1.5}In_2S_{4.5}$ could enhance the photoactivity of $Cd_{1.5}In_2S_{4.5}$. The *d* spacings of 0.32 and 0.33 nm in Fig. 2(g) correspond to the (101) crystal plane of hexagonal CdS (JCPDS No.41-1049) and the (311) crystal plane of hexagonal $CdIn_2S_4$ (JCPDS No. 27-0060), respectively; this is consistent with the XRD results. These results suggest that the synthesized photocatalyst has a polycrystalline structure. Fig. 2(g) shows that the two crystals are in close contact, which leads to formation of a heterojunction structure. This promotes the transport of photogenerated electron–hole pairs, and improves the photocatalytic activity of the material [34,35]. XRD analysis shows that $CdIn_4S_7$ is composed of $CdIn_2S_4$ and In_2S_3, but SEM images show that the two materials are not in contact (Fig. S1b). Formation of an effective heterojunction structure is therefore not possible, and the photogenerated carriers cannot be transferred across boundaries.

X-ray photoelectron spectroscopy (XPS) was used to investigate the surface chemical properties and valence states of the synthesized $Cd_{1.5}In_2S_{4.5}$ sample. The results are shown in Fig. 3. There are three main elements, i.e., S, Cd, and In, on the sample surface (Fig. 3a). The binding energies in the XP spectra were corrected with reference to the C 1s peak at 284.6 eV. The high-resolution Cd 3d, In 3d, and S 2p core-level spectra of $Cd_{1.5}In_2S_{4.5}$ are shown in Fig. 3(b)–(d). The peaks at 405.3 and 412.1 eV correspond to Cd $3d_{5/2}$ and Cd $3d_{3/2}$, respectively; this indicates that the oxidation state of the Cd ions is + 2 (Fig. 3b). The peaks at 444.9 and 452.5 eV correspond to In $3d_{5/2}$ and In $3d_{3/2}$ (Fig. 3c), respectively; this indicates that the oxidation state of the In ions is + 3. The peaks at 161.7 and 162.9 eV correspond to S $2p_{3/2}$ and S $2p_{1/2}$ (Fig. 3d), respectively; this indicates that the oxidation state of S is −2. These valences are consistent with theoretical results and literature reports [36,37]. More importantly, compared to individual $CdIn_2S_4$, the binding energies of S 2p, In 3d and Cd 2d for $Cd_{1.5}In_2S_{4.5}$ are obviously shifted to higher binding energy. The slightly positive shifts are mainly derived from the electronic interaction between $CdIn_2S_4$ and CdS. It can therefore be concluded that CdS, $CdIn_2S_4$, In_2S_3, and $Cd_xIn_yS_{(x+1.5y)}$ were successfully prepared via a one-step hydrothermal method.

3.2. Evaluation of photocatalytic performance

Fig. 4 shows the results of an experimental investigation of the oxidation of HMF to DFF with the synthesized materials as photocatalysts. The figure shows that there was little decrease in the HMF concentration after reaction for 30 min in the dark. The adsorption rate of HMF on $Cd_xIn_yS_{(x+1.5y)}$ was low. Lower adsorption allows the reaction product to leave the material surface in a timely manner. This increases opportunities for contact between the material surface and unreacted HMF, which facilitates subsequent reactions. Changing the Cd:In molar ratio used in the hydrothermal synthesis changed the photocatalytic activity in HMF oxidation. For Cd:In < 1:2, the photocatalytic activities of the materials were lower than that of pure $CdIn_2S_4$. With increasing In content, the catalytic activities of the materials became closer to that of pure In_2S_3. This may be because when Cd:In < 1:2 in the hydrothermal synthesis, In_2S_3 and $CdIn_2S_4$ do not form an effective heterojunction, and there is no synergistic effect. The photocatalytic activity was therefore lower than that of pure $CdIn_2S_4$. For Cd:In > 1:2, the catalytic activities of the materials in HMF oxidation were higher than those of pure $CdIn_2S_4$ and CdS. The DFF production rate initially increased with increasing amount of Cd and then decreased. The optimum Cd:In ratio was 1.5:2. The HMF conversion rate was 68.8%, the selectivity for DFF was 62.7%, and the DFF yield was 43.2% after 6 h. This is because of formation of an effective heterojunction between CdS nanorods and cubic $CdIn_2S_4$ crystals in the hydrothermal synthesis, as indicated by TEM images. The heterojunction structure effectively promoted the separation and transfer of photogenerated carriers, which significantly improved the photocatalytic activity. The specific details were investigated by performing electrochemical tests. When Cd:In > 1.5:2, the catalytic activities of the materials showed a downward trend. Fig. S2b shows a TEM image of $Cd_3In_2S_6$. The figure shows that when the Cd content is too large, the $CdIn_2S_4$ surface is densely covered with excess CdS nanorods, therefore the effect of $CdIn_2S_4$ is suppressed and the photocatalytic activity is poor.

Fig. S3 shows the results for several cycles of HMF selective oxidation with $Cd_{1.5}In_2S_{4.5}$ under visible light. $Cd_{1.5}In_2S_{4.5}$ still showed good degradation ability after four cycles. A comparison of the XRD patterns of the catalysts before and after the reaction (Fig. S4) shows that the crystal structure of $Cd_{1.5}In_2S_{4.5}$ did not change during the reaction. According to previous literatures [38,39], HMF might be oxidized to FDCA in the process of catalytic oxidation. Therefore, we compared the pH value before and after the photocatalytic conversion of HMF over $Cd_{1.5}In_2S_{4.5}$, and found that the pH value of the reaction solution

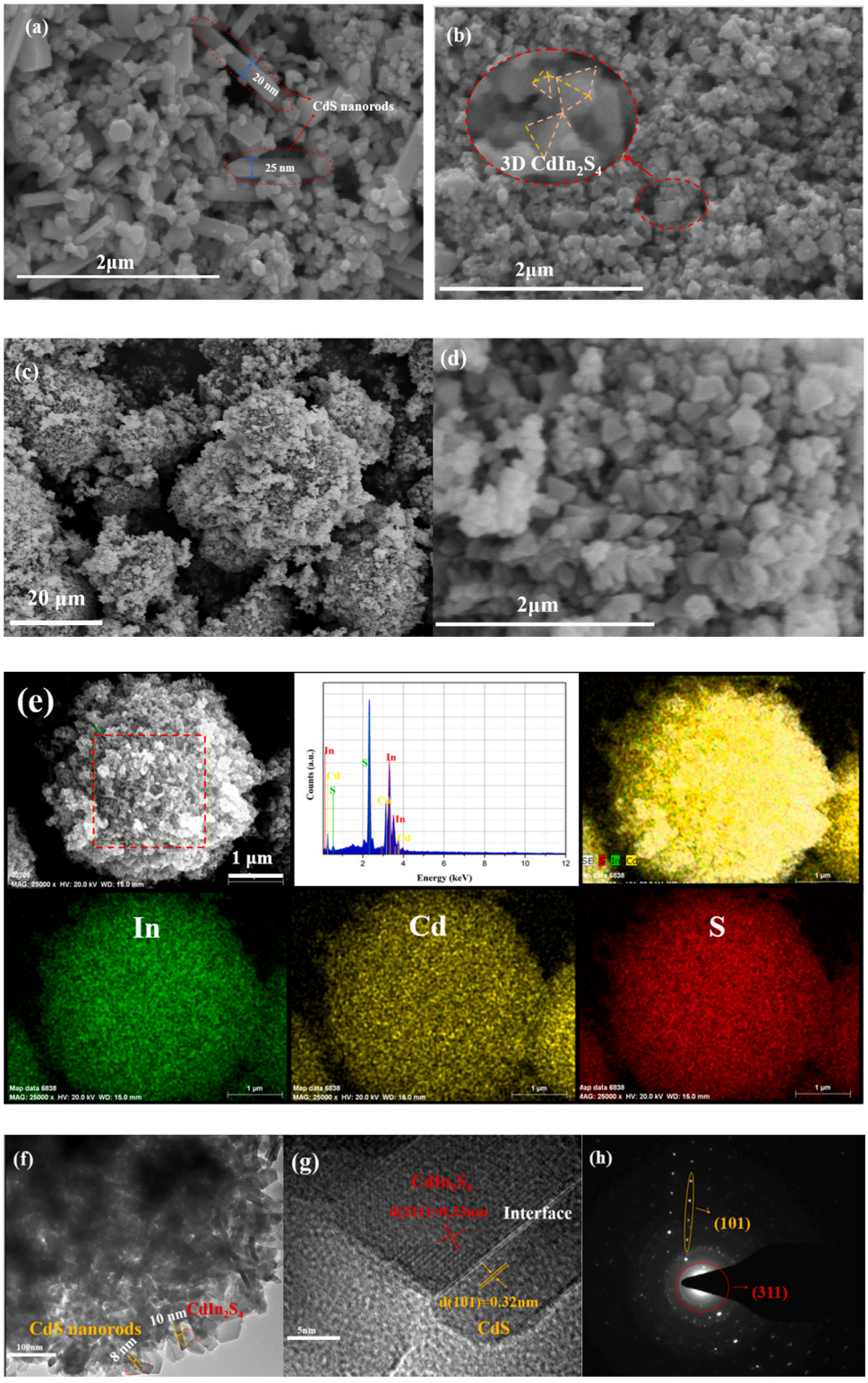

Fig. 2. SEM images of CdS (a), $CdIn_2S_4$ (b), $Cd_{1.5}In_2S_{4.5}$ (c-d), EDS pattern and EDS-mapping images of $Cd_{1.5}In_2S_{4.5}$ (e), TEM images of $Cd_{1.5}In_2S_{4.5}$ (f), HRTEM images of $Cd_{1.5}In_2S_{4.5}$ (g), HRTEM analysis results of $Cd_{1.5}In_2S_{4.5}$ (h).

decreased from 6.4 to 3.2 after 6 h, so it was reasonable to speculated that a part of organic acids was generated in the reaction process. The products of selective oxidation of HMF over $Cd_{1.5}In_2S_{4.5}$ were identified by LC-MS; the results were shown in Fig. S5. The LC-MS analysis showed that in addition to the targeted product i.e., DFF, a small amount of 2, 5-furandicarboxylic acid (FDCA , 9.8% selectivity after 6 h of photocatalysis) was formed though a further oxidation of some of the aldehyde groups in DFF to carboxyl groups.

3.3. Separation and transfer of photogenerated charge carriers

The separation and transfer efficiencies of photogenerated carriers are key factors in the photocatalytic performance [40]. The separation and transfer efficiencies of photogenerated electron–hole pairs in the

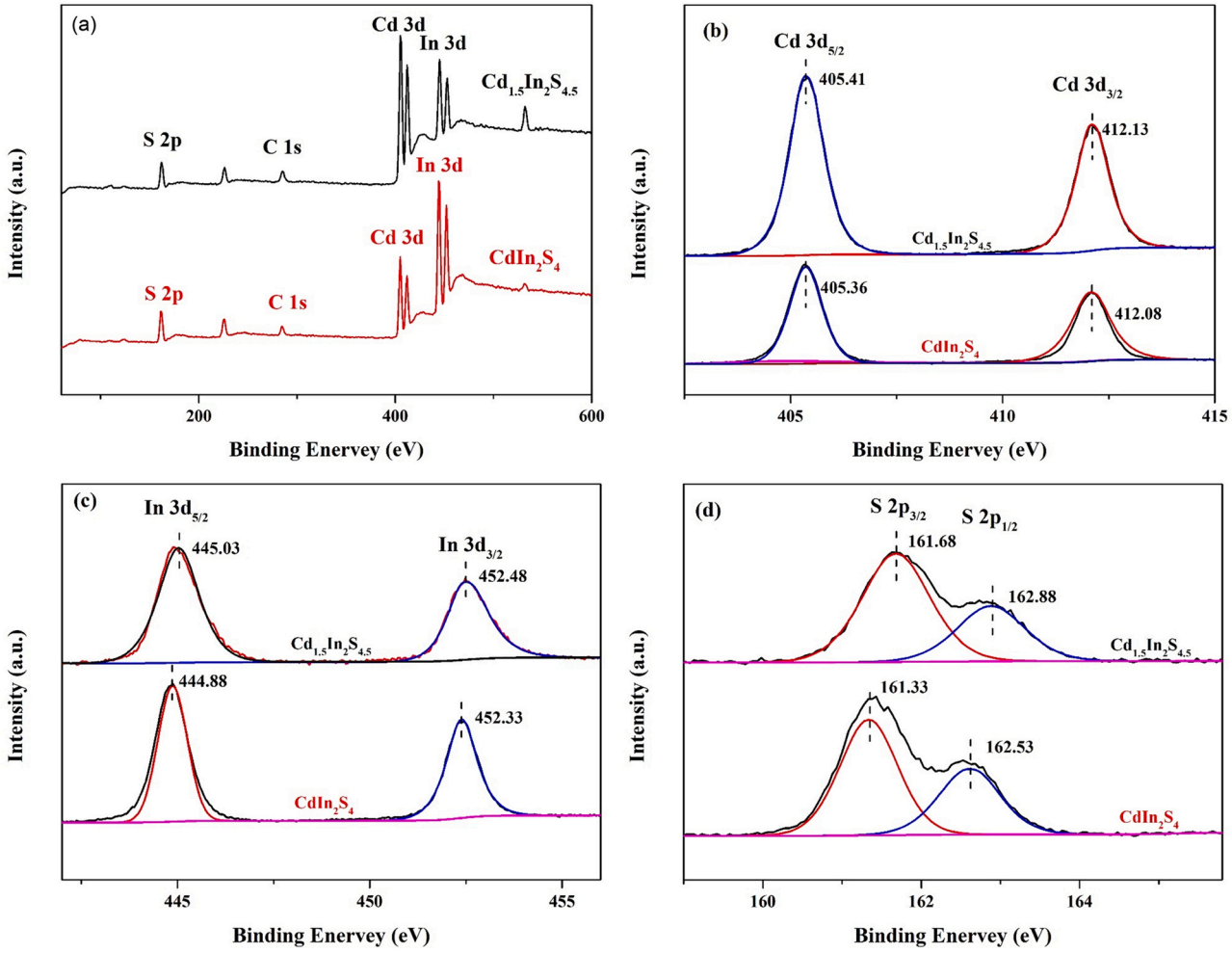

Fig. 3. XPS spectra of the resulting $Cd_{1.5}In_2S_{4.5}$ sample. Survey spectrum (a), high-resolution XPS spectra of Cd 3d (b), In 2p (c), and S 2p (d).

synthesized materials were investigated by examining the photoelectrochemical properties of CdS, In_2S_3, $CdIn_4S_7$, $CdIn_2S_4$, and $Cd_{1.5}In_2S_{4.5}$, surface photocurrent responses, and photoluminescence (PL) spectroscopy were used.

A photocurrent response is induced by separation and diffusion of photogenerated electron–hole pairs under illumination [20]. The surface photocurrent effects were investigated; the results are shown in Fig. 5(a). The figure shows that all the samples synthesized by a one-step hydrothermal method give photocurrent responses. $Cd_{1.5}In_2S_{4.5}$ clearly gives the highest photocurrent transient response. The photocurrent response of $Cd_{1.5}In_2S_{4.5}$ is approximately 1.5 and 2.9 times those of pure CdS and $CdIn_2S_4$, respectively. This indicates that the $Cd_{1.5}In_2S_{4.5}$ sample formed from one-dimensional CdS nanorods and $CdIn_2S_4$ has higher photogenerated electron–hole pair separation and transfer abilities, and the $Cd_{1.5}In_2S_{4.5}$ sample gives higher photocatalytic activity [41]. In general, a low PL intensity indicates a low electron–hole recombination rate, and a high PL intensity indicates the opposite. Fig. 5 shows the PL spectra of $Cd_{1.5}In_2S_{4.5}$, CdS, $CdIn_4S_7$, and $CdIn_2S_4$ at a 350 nm excitation wavelength. Fig. 5(b) shows that the PL intensity of $Cd_{1.5}In_2S_{4.5}$ was lower than those of CdS and $CdIn_2S_4$. This indicates that the efficiency of photogenerated electron–hole pair recombination was low. This further proves that CdS nanorods and $CdIn_2S_4$ have higher photogenerated carrier separation and transfer abilities under light conditions. In addition, Fig. 5 shows that the photocurrent response of $CdIn_4S_7$ was lower than those of the other materials, and PL intensities were higher than those of the other materials. The $CdIn_4S_7$ sample synthesized by a one-step hydrothermal method contains In_2S_3 and $CdIn_2S_4$ crystals, but there is no effective heterojunction structure between the two crystals. The photogenerated carriers do not undergo transboundary migration, which results in a low carrier migration efficiency and relatively high efficiency of photogenerated electron–hole pair recombination. This results in a low photocatalytic conversion activity.

3.4. Charge transfer pathway and photocatalytic mechanism

The optical properties of $Cd_xIn_yS_{(x+1.5y)}$ and the band structures of $CdIn_2S_4$ and CdS were investigated by UV–vis diffuse reflectance spectroscopy. Fig. 6(a) shows that the optical absorption edge of $Cd_xIn_yS_{(x+1.5y)}$ is greater than 420 nm. This shows that $Cd_xIn_yS_{(x+1.5y)}$ is visible-light-excited. The $Cd_{1.5}In_2S_{4.5}$ peak is clearly red-shifted relative to that of $CdIn_2S_4$. The bandgap energies of $CdIn_2S_4$ and CdS can be calculated by using the formula $\alpha h\nu = (h\nu - Eg)^{n/2}$, where α, A, h, E_g, and ν are the absorption coefficient, proportional coefficient, Planck's constant, bandgap energy, and optical frequency, respectively; n indicates the nature of the semiconductor transition, i.e., $n = 1$ for a direct transition, $n = 4$ for an indirect transition. According to previous reports, CdS is a direct bandgap semiconductor ($n = 1$) [30], In_2S_3 and $CdIn_2S_4$ are indirect transition conductors ($n = 4$) [33]. Therefore the values of n are 4, 4 and 1 for $CdIn_2S_4$, In_2S_3 and CdS samples, respectively. Therefore, the estimated energy band gap (Eg) values of $CdIn_2S_4$, In_2S_3 and CdS photocatalysts are 2.28, 2.18 and 2.32 eV, respectively, The band positions of the $CdIn_2S_4$ and CdS photocatalysts can be calculated by using the following empirical equations: $E_{CB} = X - 0.5E_g$

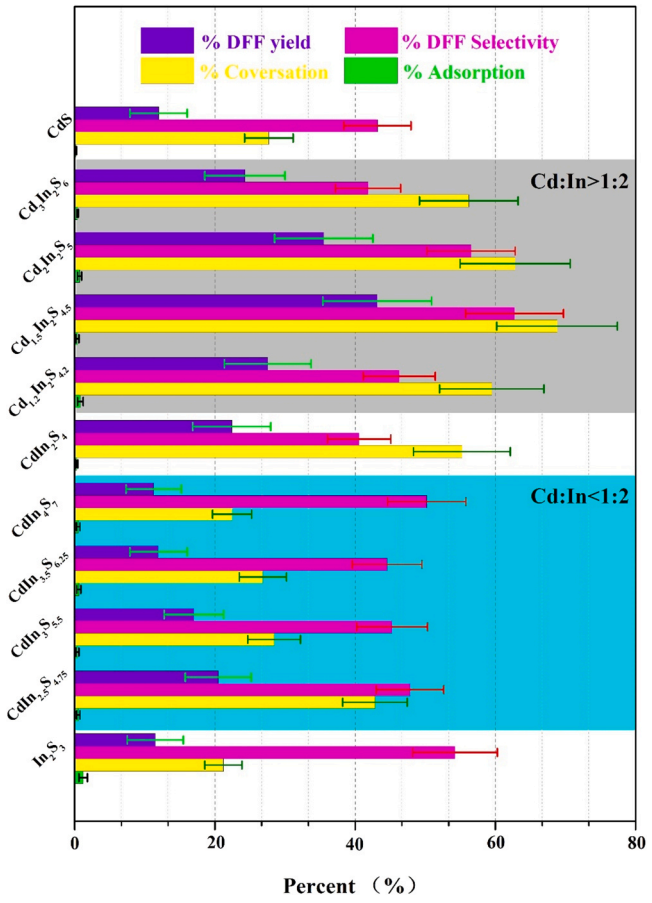

Fig. 4. Results of the oxidation of HMF under CdS, $CdIn_2S_4$, In_2S_3 and $Cd_xIn_yS_{(x+1.5y)}$ composites and adsorption rate after 30 min under dark.

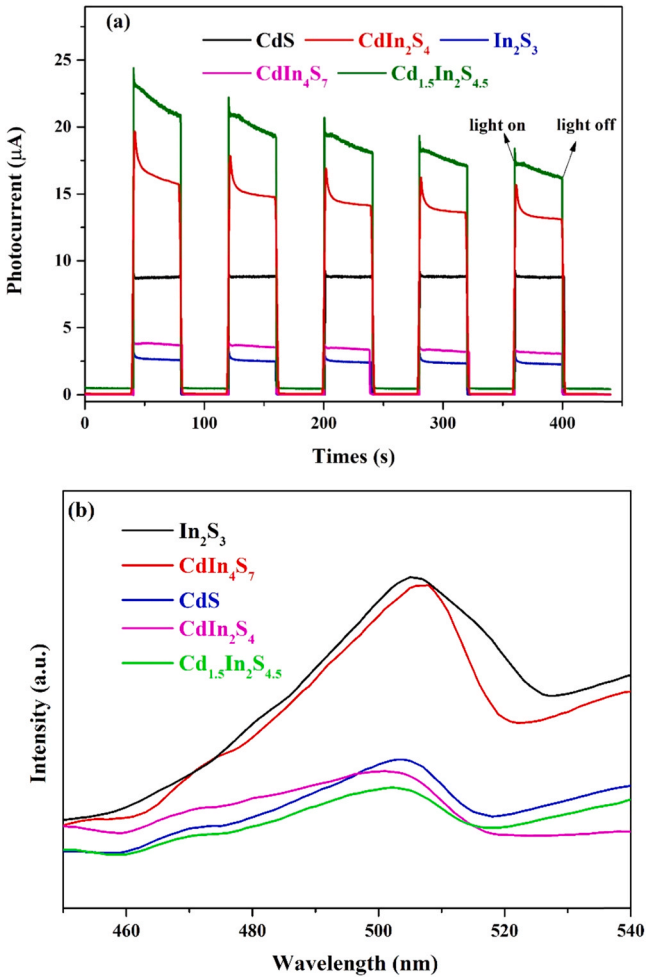

Fig. 5. Photoluminescence spectra (a) and photocurrent response (b) of different samples.

−4.5 and $E_{VB} = X + 0.5E_g$ −4.5, where E_{CB}, E_{VB}, E_g, and X are the average values of the conduction band edge, valence band edge, bandgap energy, and Mulliken electronegativity geometric values of each constituent atom, respectively. By calculation, the theoretical values of CB and VB positions are −0.80 and 1.48 eV for $CdIn_2S_4$ sample, −0.88 and 1.30 eV for In_2S_3 sample as well as −0.47 and 1.85 eV for CdS sample, respectively (Fig. 6b).

A series of control experiments were designed to clarify the process of oxidative dehydrogenation of HMF on $Cd_xIn_yS_{(x+1.5y)}$ composites. Electron (e^-)–hole (h^+) pairs are photogenerated under illumination. Photogenerated electrons combine with oxygen to form $\bullet O_2^-$, which combine with water to form hydroxyl radicals (•OH); e^-, $\bullet O_2^-$, h^+, and •OH are the main active species in photocatalytic reactions [42,43]. As shown in Fig. 7(a) and (b), hydroxyl radical and superoxide radical signals were detected in the spectra of CdS, $CdIn_2S_4$, and $Cd_{1.5}In_2S_{4.5}$. These signals were most intense in the $Cd_{1.5}In_2S_{4.5}$ spectrum, which indicates that the photoexcitation activity of $Cd_{1.5}In_2S_{4.5}$ is better than those of CdS and $CdIn_2S_4$.

Capture agent experiments were performed to identify the main active free radicals in the reaction process. Isopropanol (IPA), hydroquinone (PBQ), and ethylenediaminetetraacetic acid disodium (EDTA-2Na) are hydroxyl radical, $\bullet O_2^-$, and hole capture agents, respectively. The concentration of each capture agent in the reaction system was 10^{-4} mol/L. As shown in Table 1, IPA addition did not significantly change HMF conversion with $Cd_{1.5}In_2S_{4.5}$. When PBQ was added, catalytic conversion of HMF with $Cd_{1.5}In_2S_{4.5}$ almost stopped. When EDTA-2Na was added, HMF conversion increased by approximately 12% and the selectivity for DFF decreased by approximately 51%. Found by capture agent experiment, the HMF conversion and DFF yield were close to zero when the reaction was blocked by the addition of a $\bullet O_2^-$ capture agent. These results confirm the importance of $\bullet O_2^-$ in the reaction system, and show that holes alone cannot oxidize HMF. When a hole capture agent was added to the system, the exciton effect was weakened, and combination of the photogenerated electrons and holes was prevented, the competitive reaction of holes with EDTA-2Na decreases the recombination rate, leading to more available excess electrons for oxidative radical $\bullet O_2^-$ [44]. After hole capture, excessive superoxide anion accelerates the overoxidation of HMF, therefore the HMF conversion increases and the DFF selectivity decreases significantly. This was proved by determining the total organic carbon content and FDCA yield of the system without and with a hole capture agent (Table 1). After 6 h of reaction, the selectivity of FDCA was 9.8% and 6.9%, the carbon balance was 98.9% and 64.5%, and the furan balance was 81.1% and 36.8%, respectively. Therefore, it can be speculated that $\bullet O_2^-$ in the reaction system mainly mineralized HMF without holes, which further proved the above inference. We configured FDCA solution with the same concentration as the reaction solution, and found that its pH value was significantly higher than that of the reaction solution, so it can be proved that some complex ring-opening reactions occurred in the reaction process, and some small molecular organic acids were generated, which led to the carbon balance in the reaction system was always greater than the furan balance. It can therefore be concluded that in the photocatalytic conversion of HMF to DFF with $Cd_{1.5}In_2S_{4.5}$, $\bullet O_2^-$ plays a major role and h^+ plays a synergistic role. We compared the effects of our synthesized photocatalysts on HMF conversion to DFF with those of reported photocatalysts with $\bullet O_2^-$ as the main active species. The data in Table 2 show that $Cd_{1.5}In_2S_{4.5}$ gives an excellent performance in HMF

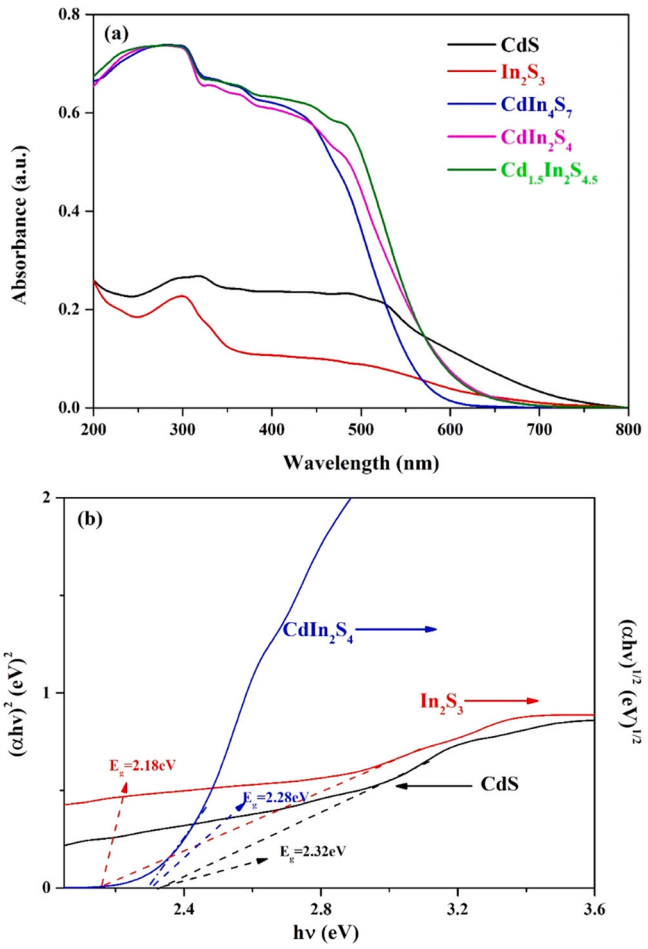

Fig. 6. (a) UV–visible diffused reflectance spectra of CdS, $CdIn_2S_4$, In_2S_3 and $Cd_xIn_yS_{(x+1.5y)}$ composites, (b) the band gaps of CdS, In_2S_3 and $CdIn_2S_4$.

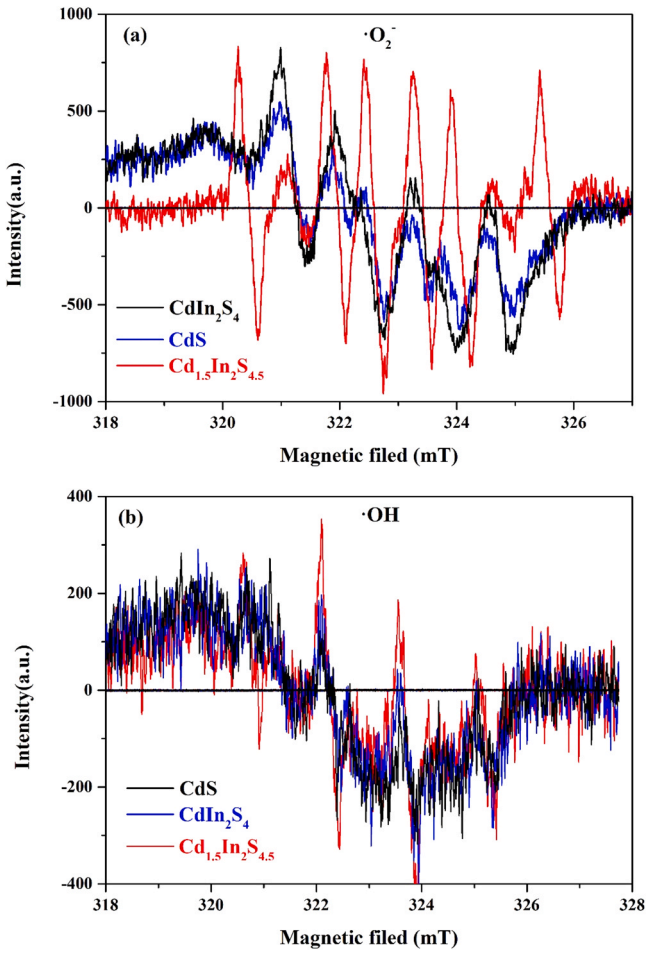

Fig. 7. ESR detection of $\bullet O_2^-$ (a) and OH^- (b) radicals under experimental conditions.

conversion.

Details of the photocatalytic conversion of HMF to DFF with $Cd_{1.5}In_2S_{4.5}$ were clarified by determining the catalytic rate at various stages of the photocatalytic conversion; the concentration of $\bullet O_2^-$ in the system was determined at 1, 3, and 5 h. Fig. 8(a) shows the reaction curve and Fig. 8(b) shows a graph of $\bullet O_2^-$ detection at 1, 3, and 5 h under dark conditions. As shown in Fig. 8(a), the reaction rate increased continuously from 1 to 3 h, reached a maximum at approximately 3 h, reached a plateau at 5 h, and then decreased significantly. Superoxide ion detection at 1, 3, and 5 h showed that the concentration of $\bullet O_2^-$ and the reaction efficiency each reached a maximum at 3 h. At 5 h, the concentration of $\bullet O_2^-$ decreased significantly, and the reaction reached a plateau. The initial increase and the subsequent decrease in the $\bullet O_2^-$ concentration may be attributed to the fact that, at the beginning of the reaction, the oxygen molecules in the reaction system were transformed into $\bullet O_2^-$ by the photocatalyst under illumination. The concentration of $\bullet O_2^-$ in the solution gradually increased, and the reaction rate also increased. When the reaction time was approximately 5 h, most of the oxygen molecules in the reaction system had been consumed, and the concentration of oxygen molecules decreased. This led to a decrease in the concentration of $\bullet O_2^-$ as the active species in the system and a decrease in the reaction rate. However, after a certain reaction time, water molecules formed hydrogen bonds on the surface of the catalyst, which blocked contact between HMF molecules and the active sites on the catalyst surface. This resulted in a gradual decrease in the conversion rate and a decrease in the activity of the catalyst [24]. The importance of oxygen in the reaction system was confirmed by introducing nitrogen, to make the reaction system anaerobic. No product was obtained after 6 h of illumination. This verifies that the selective oxidation of HMF was closely related to the presence of $\bullet O_2^-$.

XRD and TEM results showed that $Cd_{1.5}In_2S_{4.5}$ has a heterojunction structure, which is constructed from CdS nanorods and cubic $CdIn_2S_4$. The CdS nanorods can achieve long-distance charge separation because of their radial quantum confinement and axial blocking characteristics, which promote the transfer of photogenerated carriers between CdS nanorods and cubic $CdIn_2S_4$. UV–vis spectroscopy showed that the bandgap of $CdIn_2S_4$ is 2.28 eV, and the theoretical potentials of the conduction and valence bands are −0.80 and 1.48 eV, respectively. The CdS bandgap is 2.32 eV, and the theoretical potentials of the conduction and valence bands are −0.47 and 1.85 eV, respectively. The potential of the $CdIn_2S_4$ conduction band is significantly lower than that of the CdS valence band. When $Cd_{1.5}In_2S_{4.5}$ is exposed to visible light, photoinduced electrons and holes are generated on the surfaces of CdS nanorods and cubic $CdIn_2S_4$. The electrons photogenerated by $CdIn_2S_4$ spontaneously move from the conduction band of $CdIn_2S_4$ through the contact surface to the conduction band of CdS. This achieves transboundary transfer of photogenerated carriers in space. ESR spectra and trapping agent experiments showed that, in this system, the selective oxidation of HMF to DFF occurs via the combined actions of oxygen molecules, photogenerated electrons, superoxide anions, and holes. When the photocatalytic reaction starts, HMF molecules first contact holes to form alcohol oxygen anion radicals and H^+. Photogenerated electrons combine with oxygen molecules to form $\bullet O_2^-$. Contact between H^+ and $\bullet O_2^-$ forms •OOH, which further oxidizes the alcohol oxygen anion radicals to produce DFF and $H_2O_2{\cdot}H_2O_2$ can further oxidize the aldehyde groups of DFF to FDCA. In order to further verify our hypothesis, we

Table 1
The influence of various scavengers on the photocatalytic reaction behavior [a].

catalysis	scavengers	light source	HMF conv. (%)	DFF sel. (%)	FDCA sel. (%)	pH[b]	carbon balance (%)	furan balance (%)
$Cd_{1.5}In_2S_{4.5}$	no	xenon lamp(λ > 420 nm)	68.8	62.7	9.8	3.5	98.9	81.1
$Cd_{1.5}In_2S_{4.5}$	no	dark	0	0	0	6.3	100	100
$Cd_{1.5}In_2S_{4.5}$	IPA	xenon lamp(λ > 420 nm)	66.4	63.2	9.4	3.6	99.1	81.8
$Cd_{1.5}In_2S_{4.5}$	PBQ	xenon lamp(λ > 420 nm)	1.2	64.5	0	6.2	99.8	98.8
$Cd_{1.5}In_2S_{4.5}$	EDTA-2Na	xenon lamp(λ > 420 nm)	80.2	14.3	6.9	2.8	64.5	36.8
$Cd_{1.5}In_2S_{4.5}$	catalase	xenon lamp(λ > 420 nm)	67.4	68.3	1.9	5.2	99.5	79.9
H_2O_2[c]	no	xenon lamp(λ > 420 nm)	0	0	0	4.1	100	100

[a] Reaction conditions: HMF solution (5 mL, 4 mg/mL), 20 mg of photocatalyst, 20 ℃, air, 6 h, the concentration of each capture agent in the reaction system was 10^{-4} mol/L.
[b] The pH value in the solution after 6 h of reaction was shown in the table. The initial pH value was 6.1–6.4.
[c] Reaction conditions: HMF solution (5 mL, 4 mg/mL), 5 mmol H_2O_2, 20 ℃, air and 6 h.

Table 2
Comparison of herein reported HMF oxidation to DFF results with other photocatalysts with $\bullet O_2^-$ as the main active factor.

Catalyst	Solvent	Reaction conditions	Conv. (%)	Select. (%)	Yield (%)	Ref.
$Cd_{1.5}In_2S_{4.5}$	Water	500 W Xe lamp (λ > 420 nm), 20 ℃ , under air	68.8	62.7	43.2	This work
N-TiO_2	Water	500 W lamp (λ = 365 nm), 20 ℃, under air	–	30.0–40.0	–	[45]
g-C_3N_4	Water	Sunlight, 25 ℃, under air	40.0	50.0	20.0	[18]
g-C_3N_4-H_2O_2	Water	Sunlight, 20 ℃, under air	20.0	88.0	17.6	[46]
WO_3/g-C_3N_4	ACN+$PhCF_3$	Xe lamp (λ > 400 nm), 30 ℃, O_2 purging	27.4	87.2	23.9	[47]

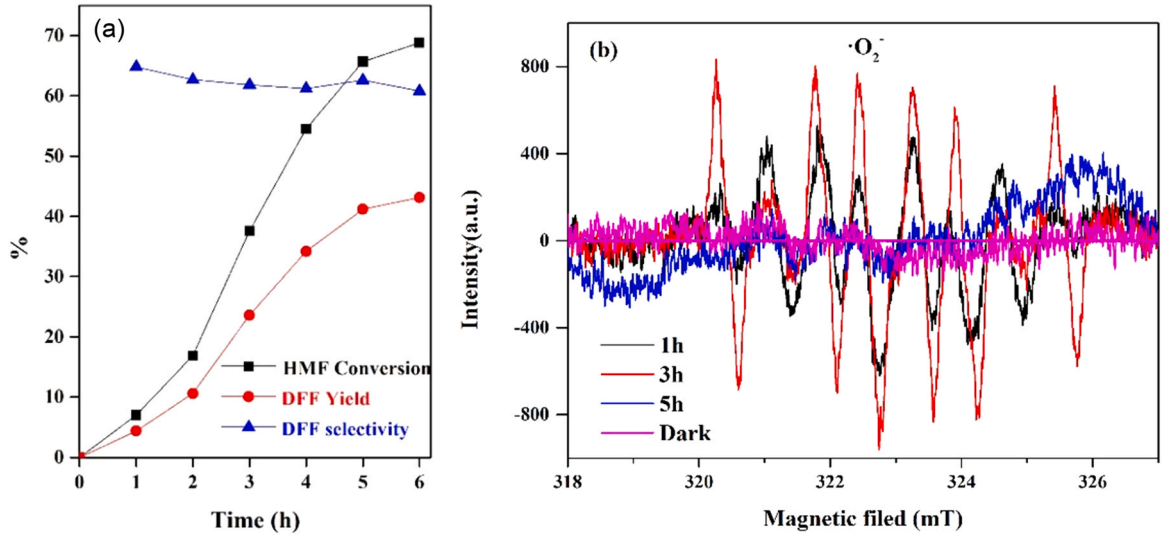

Fig. 8. The evolution of HMF conversion and DFF Yield with time (a), the evolution of $\bullet O_2^-$ concentration with time (b).

quantitatively analyzed the important product H_2O_2 produced in the reaction process (0.5 mL sample + 0.5 mL sulfuric acid (0.5 M) + 0.05 mL titanium sulfate + 3.95 mL water, mixed evenly, measured absorbance at 410 nm wavelength). Under standard conditions (20 mg of $Cd_{1.5}In_2S_{4.5}$, HMF solution (5 mL, 4 mg/mL), air, 6 h, xenon lamp (λ > 420 nm)), H_2O_2 was not produced after 30 min of dark reaction and 3.2 mmol/L H_2O_2 was produced after 6 h of photocatalytic reaction (Fig. S6). Considering the possibility that H_2O_2 may also act as a potential oxidant for the oxidation reaction [21]. We added catalase to the reaction solution under standard conditions, after 6 h of reaction, the pH value of the solution (5.3) was higher than that under the standard condition for 6 h (3.2). The selectivity of FDCA decreased to 1.9%, and the selectivity of DFF increased by about 5.6% (Table 1). The addition of up to 10 mmol H_2O_2 to the catalytic solution in the absence of $Cd_{1.5}In_2S_{4.5}$ does not cause any oxidation of HMF after 6 h irradiation. These results clearly revealed that the generated H_2O_2 did not play a crucial role in the photocatalytic oxidation process. The important role of $\bullet O_2^-$ and h^+ in $Cd_{1.5}In_2S_{4.5}$ catalytic oxidation of HMF to DFF system was further proved. Fig. 9 shows a possible mechanism for the photocatalytic conversion of HMF to DFF with $Cd_{1.5}In_2S_{4.5}$.

4. Conclusion

$CdIn_2S_4$, In_2S_3, CdS and $Cd_xIn_yS_{(x+1.5y)}$ photocatalysts were prepared by a one-step hydrothermal method. These photocatalysts can selectively convert HMF to high-value-added fine chemicals, e.g., DFF, under

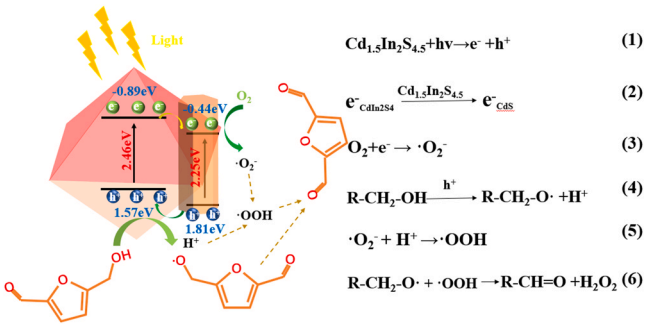

Fig. 9. Illustrated representation of the light effect and the involved oxidation mechanism of HMF over $Cd_{1.5}In_2S_{4.5}$.

mild conditions. For Cd:In > 1:2, three-dimensional $Cd_xIn_yS_{(x+1.5y)}$ microspheres composed of one-dimensional CdS nanorods and cubic $CdIn_2S_4$ were formed. The material with Cd:In= 1.5:2 had the highest activity, and the DFF yield reached 43.2%, this is 3.64 and 1.92 times those achieved with pure CdS and $CdIn_2S_4$, respectively. XRD, SEM, and TEM investigations showed that one-dimensional CdS nanorods and cubic $CdIn_2S_4$ can form an effective heterojunction. Surface photocurrent and PL spectra calculations showed that one-dimensional CdS nanorods effectively promoted the migration and separation of photogenerated carriers, and improved the HMF catalytic conversion efficiency of the $Cd_xIn_yS_{(x+1.5y)}$ materials. A reasonable photocatalytic reaction mechanism was proposed on the basis of UV–vis, ESR, and capture agent experiments. The results of this study show that cadmium–indium sulfides have potential applications in the photocatalytic conversion of biomass to value-added chemicals, and provide a method for constructing efficient visible-light-driven composite photocatalysts from one-dimensional CdS nanorods.

CRediT authorship contribution statement

Ming Zhang: Investigation, Methodology, Writing – original draft. **Zhihao Yu:** Conceptualization, Revision, Project administration. **Jian Xiong:** Formal analysis, Resources, Supervision. **Rui Zhang:** Supervision, Resources, Project administration. **Xinzhong Liu:** Formal analysis, Supervision. **Xuebin Lu:** Conceptualization, Funding acquisition, Project administration, Resources, Supervision, Validation, Visualization.

Declaration of Competing Interest

The authors declare that they have no known competing financial interests or personal relationships that could have appeared to influence the work reported in this paper.

Acknowledgements

This work was supported by the National Natural Science Foundation of China (Grant Nos. 52066017, 51876180, 51908400), Tibet University 2019 Central Financial Support Special Funds for Local Colleges and Universities (Grant No. 1), 2021 Wuhan University of Technology-Tibet University "Tibetan Economic and Social Development and Plateau Scientific Research Co-construction Innovation Fund" Special Project (Grant No. lzj2021004), Everest Discipline Construction Project of Tibet University (Grant No. ZF21000002).

Appendix A. Supporting information

Supplementary data associated with this article can be found in the online version at doi:10.1016/j.apcatb.2021.120738.

References

[1] C. Li, Y. Na, Recent advances in photocatalytic oxidation of 5–hydroxymethylfurfural, ChemPhotoChem 5 (2021) 502–511, https://doi.org/10.1002/cptc.202000261.
[2] X. Wu, N. Luo, S. Xie, H. Zhang, Q. Zhang, F. Wang, Y. Wang, Photocatalytic transformations of lignocellulosic biomass into chemicals, Chem. Soc. Rev. 49 (2020) 6198–6223, https://doi.org/10.1039/d0cs00314j.
[3] L. Hu, J. Xu, S. Zhou, A. He, X. Tang, L. Lin, J. Xu, Y. Zhao, Catalytic advances in the production and application of biomass-derived 2,5-dihydroxymethylfuran, ACS Catal. 8 (2018) 2959–2980, https://doi.org/10.1021/acscatal.7b03530.
[4] X. Kong, Y. Zhu, Z. Fang, J.A. Kozinski, I.S. Butler, L. Xu, H. Song, X. Wei, Catalytic conversion of 5-hydroxymethylfurfural to some value-added derivatives, Green Chem. 20 (2018) 3657–3682, https://doi.org/10.1039/c8gc00234g.
[5] M.J. Climent, A. Corma, S. Iborra, Conversion of biomass platform molecules into fuel additives and liquid hydrocarbon fuels, Green Chem. 16 (2014) 516, https://doi.org/10.1039/c3gc41492b.
[6] L. Hu, A. He, X. Liu, J. Xia, J. Xu, S. Zhou, J. Xu, Biocatalytic transformation of 5-hydroxymethylfurfural into high-value derivatives: recent advances and future aspects, ACS Sustain. Chem. Eng. 6 (2018) 15915–15935, https://doi.org/10.1021/acssuschemeng.8b04356.
[7] J. Ma, Z. Du, J. Xu, Q. Chu, Y. Pang, Efficient aerobic oxidation of 5-hydroxymethylfurfural to 2,5-diformylfuran, and synthesis of a fluorescent material, ChemSusChem 4 (2011) 51–54, https://doi.org/10.1002/cssc.201000273.
[8] T. Cao, M. Wu, V.V. Ordomsky, X. Xin, H. Wang, P. Metivier, M. Pera-Titus, Selective electrogenerative oxidation of 5-hydroxymethylfurfural to 2,5-furandialdehyde, ChemSusChem 10 (2017) 4851–4854, https://doi.org/10.1002/cssc.201702119.
[9] P. Kisszekelyi, R. Hardian, H. Vovusha, B. Chen, X. Zeng, U. Schwingenschlogl, J. Kupai, G. Szekely, Selective electrocatalytic oxidation of biomass-derived 5-hydroxymethylfurfural to 2,5-diformylfuran: from mechanistic investigations to catalyst recovery, ChemSusChem 13 (2020) 3060, https://doi.org/10.1002/cssc.202001276.
[10] Y. Liu, L. Zhu, J. Tang, M. Liu, R. Cheng, C. Hu, One-pot, one-step synthesis of 2,5-diformylfuran from carbohydrates over Mo-containing Keggin heteropolyacids, ChemSusChem 7 (2014) 3541–3547, https://doi.org/10.1002/cssc.201402468.
[11] G.D. Yadav, R.V. Sharma, Biomass derived chemicals: environmentally benign process for oxidation of 5-hydroxymethylfurfural to 2,5-diformylfuran by using nano-fibrous Ag-OMS-2-catalyst, Appl. Catal. B. 147 (2014) 293–301, https://doi.org/10.1016/j.apcatb.2013.09.004.
[12] W.-D. Oh, G. Lisak, R.D. Webster, Y.-N. Liang, A. Veksha, A. Giannis, J.G.S. Moo, J.-W. Lim, T.-T. Lim, Insights into the thermolytic transformation of lignocellulosic biomass waste to redox-active carbocatalyst: durability of surface active sites, Appl. Catal. B 233 (2018) 120–129, https://doi.org/10.1016/j.apcatb.2018.03.106.
[13] Y. Fu, L. Sun, H. Yang, L. Xu, F. Zhang, W. Zhu, Visible-light-induced aerobic photocatalytic oxidation of aromatic alcohols to aldehydes over Ni-doped NH 2 -MIL-125(Ti), Appl. Catal. B 187 (2016) 212–217, https://doi.org/10.1016/j.apcatb.2016.01.038.
[14] D. Zhao, T. Su, Y. Wang, R.S. Varma, C. Len, Recent advances in catalytic oxidation of 5-hydroxymethylfurfural, Mol. Catal. 495 (2020), 111133, https://doi.org/10.1016/j.mcat.2020.111133.
[15] X. Wu, S. Xie, H. Zhang, Q. Zhang, B.F. Sels, Y. Wang, Metal sulfide photocatalysts for lignocellulose valorization, Adv. Mater. (2021), 2007129, https://doi.org/10.1002/adma.202007129.
[16] L. Marzo, S.K. Pagire, O. Reiser, B. Konig, Visible-light photocatalysis: does it make a difference in organic synthesis? Angew. Chem. Int. Ed. Engl. 57 (2018) 10034–10072, https://doi.org/10.1002/anie.201709766.
[17] L.I. Granone, F. Sieland, N. Zheng, R. Dillert, D.W. Bahnemann, Photocatalytic conversion of biomass into valuable products: a meaningful approach? Green Chem. 20 (2018) 1169–1192, https://doi.org/10.1039/c7gc03522e.
[18] I. Krivtsov, E.I. García-López, G. Marcì, L. Palmisano, Z. Amghouz, J.R. García, S. Ordóñez, E. Díaz, Selective photocatalytic oxidation of 5-hydroxymethyl-2-furfural to 2,5-furandicarboxyaldehyde in aqueous suspension of g-C_3N_4, Appl. Catal. B 204 (2017) 430–439, https://doi.org/10.1016/j.apcatb.2016.11.049.
[19] X. Wu, J. Li, S. Xie, P. Duan, H. Zhang, J. Feng, Q. Zhang, J. Cheng, Y. Wang, Selectivity control in photocatalytic valorization of biomass-derived platform compounds by surface engineering of titanium oxide, Chem 6 (2020) 3038–3053, https://doi.org/10.1016/j.chempr.2020.08.014.
[20] S. Meng, H. Wu, Y. Cui, X. Zheng, H. Wang, S. Chen, Y. Wang, X. Fu, One-step synthesis of 2D/^{2}D–^{3}D NiS/$Zn_3In_2S_6$ hierarchical structure toward solar-to-chemical energy transformation of biomass-relevant alcohols, Appl. Catal. B: Environ. 266 (2020), 118617, https://doi.org/10.1016/j.apcatb.2020.118617.
[21] M. Zhang, Z. Li, X. Xin, J. Zhang, Y. Feng, H. Lv, Selective valorization of 5-hydroxymethylfurfural to 2,5-diformylfuran using atmospheric O_2 and MAPbBr3 perovskite under visible light, ACS Catal. 10 (2020) 14793–14800, https://doi.org/10.1021/acscatal.0c04330.
[22] S. Yurdakal, B.S. Tek, O. Alagöz, V. Augugliaro, V. Loddo, G. Palmisano, L. Palmisano, Photocatalytic selective oxidation of 5-(Hydroxymethyl)-2-furaldehyde to 2,5-furandicarbaldehyde in water by using anatase, rutile, and brookite TiO_2 nanoparticles, ACS Sustain. Chem. Eng. 1 (2013) 456–461, https://doi.org/10.1021/sc300142a.
[23] H. Zhang, Q. Wu, C. Guo, Y. Wu, T. Wu, Photocatalytic selective oxidation of 5-hydroxymethylfurfural to 2,5-diformylfuran over Nb_2O_5 under visible light, ACS Sustain. Chem. Eng. 5 (2017) 3517–3523, https://doi.org/10.1021/acssuschemeng.7b00231.

[24] D.A. Giannakoudakis, V. Nair, A. Khan, E.A. Deliyanni, J.C. Colmenares, K. S. Triantafyllidis, Additive-free photo-assisted selective partial oxidation at ambient conditions of 5-hydroxymethylfurfural by manganese (IV) oxide nanorods, Appl. Catal. B: Environ. 256 (2019), 117803, https://doi.org/10.1016/j.apcatb.2019.117803.

[25] G. Han, Y.H. Jin, R.A. Burgess, N.E. Dickenson, X.M. Cao, Y. Sun, Visible-light-driven valorization of biomass intermediates integrated with H_2 production catalyzed by ultrathin Ni/CdS nanosheets, J. Am. Chem. Soc. 139 (2017) 15584–15587, https://doi.org/10.1021/jacs.7b08657.

[26] M.D. Regulacio, M.Y. Han, Multinary I-III-VI2 and I2-II-IV-VI4 semiconductor nanostructures for photocatalytic applications, Acc. Chem. Res. 49 (2016) 511–519, https://doi.org/10.1021/acs.accounts.5b00535.

[27] P. Zhang, S. Wang, B.Y. Guan, X.W. Lou, Fabrication of CdS hierarchical multi-cavity hollow particles for efficient visible light CO_2 reduction, Energy Environ. Sci. 12 (2019) 164–168, https://doi.org/10.1039/c8ee02538j.

[28] G. Hautier, A. Miglio, G. Ceder, G.M. Rignanese, X. Gonze, Identification and design principles of low hole effective mass p-type transparent conducting oxides, Nat. Commun. 4 (2013) 2292, https://doi.org/10.1038/ncomms3292.

[29] C.M. Wolff, P.D. Frischmann, M. Schulze, B.J. Bohn, R. Wein, P. Livadas, M. T. Carlson, F. Jäckel, J. Feldmann, F. Würthner, J.K. Stolarczyk, All-in-one visible-light-driven water splitting by combining nanoparticulate and molecular co-catalysts on CdS nanorods, Nat. Energy 3 (2018) 862–869, https://doi.org/10.1038/s41560-018-0229-6.

[30] L. Cheng, Q. Xiang, Y. Liao, H. Zhang, CdS-based photocatalysts, Energy Environ. Sci. 11 (2018) 1362–1391, https://doi.org/10.1039/c7ee03640j.

[31] W. Wang, T.W. Ng, W.K. Ho, J. Huang, S. Liang, T. An, G. Li, J.C. Yu, P.K. Wong, $CdIn_2S_4$ microsphere as an efficient visible-light-driven photocatalyst for bacterial inactivation: synthesis, characterizations and photocatalytic inactivation mechanisms, Appl. Catal. B 129 (2013) 482–490, https://doi.org/10.1016/j.apcatb.2012.09.054.

[32] S.K. Apte, S.N. Garaje, R.D. Bolade, J.D. Ambekar, M.V. Kulkarni, S.D. Naik, S. W. Gosavi, J.O. Baeg, B.B. Kale, Hierarchical nanostructures of $CdIn_2S_4$via hydrothermal and microwave methods: efficient solar-light-driven photocatalysts, J. Mater. Chem. 20 (2010) 6095, https://doi.org/10.1039/c0jm00538j.

[33] X. Ye, Y. Chen, C. Ling, J. Zhang, S. Meng, X. Fu, X. Wang, S. Chen, Chalcogenide photocatalysts for selective oxidation of aromatic alcohols to aldehydes using O_2 and visible light: a case study of $CdIn_2S_4$, CdS and In_2S_3, Chem. Eng. J. 348 (2018) 966–977, https://doi.org/10.1016/j.cej.2018.05.035.

[34] A. Meng, B. Zhu, B. Zhong, L. Zhang, B. Cheng, Direct Z-scheme TiO_2/CdS hierarchical photocatalyst for enhanced photocatalytic H_2-production activity, Appl. Surf. Sci. 422 (2017) 518–527, https://doi.org/10.1016/j.apsusc.2017.06.028.

[35] T. Wang, D. Yue, X. Li, Y. Zhao, Lead-free double perovskite $Cs_2AgBiBr_6$/RGO composite for efficient visible light photocatalytic H_2 evolution, Appl. Catal. B: Environ. 268 (2020), 118399, https://doi.org/10.1016/j.apcatb.2019.118399.

[36] S. Wang, B. Zhu, M. Liu, L. Zhang, J. Yu, M. Zhou, Direct Z-scheme ZnO/CdS hierarchical photocatalyst for enhanced photocatalytic H_2-production activity, Appl. Catal. B. 243 (2019) 19–26, https://doi.org/10.1016/j.apcatb.2018.10.019.

[37] S. Guo, Y. Li, C. Xue, Y. Sun, C. Wu, G. Shao, P. Zhang, Controllable construction of hierarchically $CdIn_2S_4$/CNFs/Co_4S_3 nanofiber networks towards photocatalytic hydrogen evolution, Chem. Eng. J. 419 (2021), 129213, https://doi.org/10.1016/j.cej.2021.129213.

[38] D.A. Giannakoudakis, J.C. Colmenares, D. Tsiplakides, K.S. Triantafyllidis, Nanoengineered electrodes for biomass-derived 5-hydroxymethylfurfural electrocatalytic oxidation to 2,5-furandicarboxylic acid, ACS Sustain. Chem. Eng. 9 (2021) 1970–1993, https://doi.org/10.1021/acssuschemeng.0c07480.

[39] L. Gao, Z. Liu, J. Ma, L. Zhong, Z. Song, J. Xu, S. Gan, D. Han, L. Niu, NiSe@NiOx core-shell nanowires as a non-precious electrocatalyst for upgrading 5-hydroxymethylfurfural into 2,5-furandicarboxylic acid, Appl Catal. B 261 (2020), 118235, https://doi.org/10.1016/j.apcatb.2019.118235.

[40] J. Low, J. Yu, M. Jaroniec, S. Wageh, A.A. Al-Ghamdi, Heterojunction photocatalysts, Adv. Mater. 29 (2017), https://doi.org/10.1002/adma.201601694.

[41] Q. Zhang, J. Wang, X. Ye, Z. Hui, L. Ye, X. Wang, S. Chen, Self-assembly of CdS/$CdIn_2S_4$ heterostructure with enhanced photocascade synthesis of schiff base compounds in an aromatic alcohols and nitrobenzene system with visible light, ACS Appl. Mater. Interfaces 11 (2019) 46735–46745, https://doi.org/10.1021/acsami.9b14450.

[42] Z. Shayegan, C.-S. Lee, F. Haghighat, TiO_2 photocatalyst for removal of volatile organic compounds in gas phase – a review, Chem. Eng. J. 334 (2018) 2408–2439, https://doi.org/10.1016/j.cej.2017.09.153.

[43] Z. Wang, C. Li, K. Domen, Recent developments in heterogeneous photocatalysts for solar-driven overall water splitting, Chem. Soc. Rev. 48 (2019) 2109–2125, https://doi.org/10.1039/c8cs00542g.

[44] S. Ghosh, N.A. Kouame, L. Ramos, S. Remita, A. Dazzi, A. Deniset-Besseau, P. Beaunier, F. Goubard, P.H. Aubert, H. Remita, Conducting polymer nanostructures for photocatalysis under visible light, Nat. Mater. 14 (2015) 505–511, https://doi.org/10.1038/nmat4220.

[45] I. Krivtsov, M. Ilkaeva, E. Salas-Colera, Z. Amghouz, J.R. García, E. Díaz, S. Ordóñez, S. Villar-Rodil, Consequences of nitrogen doping and oxygen enrichment on titanium local order and photocatalytic performance of TiO_2 anatase, J. Phys. Chem. C 121 (2017) 6770–6780, https://doi.org/10.1021/acs.jpcc.7b00354.

[46] M. Ilkaeva, I. Krivtsov, E.I. García-López, G. Marcì, O. Khainakova, J.R. García, L. Palmisano, E. Díaz, S. Ordóñez, Selective photocatalytic oxidation of 5-hydroxymethylfurfural to 2,5-furandicarboxaldehyde by polymeric carbon nitride-hydrogen peroxide adduct, J. Catal. 359 (2018) 212–222, https://doi.org/10.1016/j.jcat.2018.01.012.

[47] H. Zhang, Z. Feng, Y. Zhu, Y. Wu, T. Wu, Photocatalytic selective oxidation of biomass-derived 5-hydroxymethylfurfural to 2,5-diformylfuran on WO_3/g-C_3N_4 composite under irradiation of visible light, J. Photochem. Photobiol. A 371 (2019) 1–9, https://doi.org/10.1016/j.jphotochem.2018.10.044.